







Canted antiferromagnetism and spin reorientation in corner-shared single chain quasi-one-dimensional Ba₂FeSe₃

Fei Gao ^{1,*}, Nikhil Dhale,^{1,*} Ling-Fang Lin ^{2,*}, Keith M. Taddei ^{3,4}, Yang Zhang ⁵, Clarina Dela Cruz,³ Elbio Dagotto ^{2,5} and Bing Lv ^{1,6,†}

¹Department of Physics, *University of Texas at Dallas*, Richardson, Texas 75080, USA

²Department of Physics and Astronomy, *University of Tennessee*, Knoxville, Tennessee 37996, USA

³Neutron Scattering Division, *Oak Ridge National Laboratory*, Oak Ridge, Tennessee 37831, USA

⁴X-ray Science Division, *Argonne National Laboratory*, Lemont, Illinois 60439, USA

⁵Materials Science and Technology Division, *Oak Ridge National Laboratory*, Oak Ridge, Tennessee 37831, USA

⁶Department of Materials Science and Engineering, *University of Texas at Dallas*, Richardson, Texas 75080, USA



(Received 17 November 2025; revised 9 January 2026; accepted 13 January 2026; published 11 February 2026)

We report the canted antiferromagnetic (AFM) structure together with a spin reorientation in a single chain quasi-one-dimensional (Q-1D) iron chalcogenide Ba₂FeSe₃. Ba₂FeSe₃ crystallizes in *Pnma* (No. 62) orthorhombic structure with linear single iron chains consisting of corner-shared distorted FeSe₄ tetrahedra along the *b* axis. Ba₂FeSe₃ is a narrow-gap semiconductor and orders AFM below 60 K. Modeling of neutron powder diffraction data reveals a canted AFM ground state of magnetic space group *Pa21/c* (BNS No. 14.80) with commensurate propagation vector $\mathbf{k} = (0, \frac{1}{2}, 0)$, where the Fe ion spins are AFM aligned with up-down-up-down ($\uparrow - \downarrow - \uparrow - \downarrow$) sequence along the Q-1D chain direction of the *b* axis. In the magnetically ordered state, the canting of magnetic moments reorients from the *ac* plane to the *ab* plane below 30 K, with a 10° tilting angle toward the *a* axis, and the magnetic moment does not induce a net moment in either orientation. The density functional theory results indicate that an $\uparrow - \downarrow - \uparrow - \downarrow$ AFM state is stabilized along the chain direction. In this work, we elucidate the unique canted AFM of the iron chalcogenide and pave the way for searching exotic physics in Q-1D Ba₂FeSe₃.

DOI: [10.1103/1b28-p1fr](https://doi.org/10.1103/1b28-p1fr)

I. INTRODUCTION

The discovery of iron-based superconductors [1–4] triggered significant research interest in studying the intriguing interplay between superconductivity and magnetism [5–9]. Many parent compounds of iron-based superconductors are poor metals exhibiting antiferromagnetic (AFM) ordering at low temperatures [5–12], with magnetic order manifesting in various forms [13–15]. Despite the central role of stripelike magnetic orders in the physics of high-temperature superconductors [16,17], the inherently three-dimensional (3D) or two-dimensional (2D) nature of their crystal structures presents significant challenges for experimental investigation [2,3,18–21]. The Fe-based superconducting phases are typically stabilized within quasi-2D (Q-2D) layers composed of FeAs or FeSe structural units, where Fe atoms are tetrahedrally coordinated, forming FeAs₄ or FeSe₄ motifs [2,3,10,18,19,22,23]. Therefore, exploring iron-based compounds in lower dimensions, e.g., quasi-one-dimensional (Q-1D) forms that incorporate the same tetrahedra structural building blocks and meanwhile simultaneously exhibit AFM order, will offer a promising strategy for understanding high-temperature superconductivity and potentially discovering superconducting phases [24–26].

1D materials, due to their strongly constrained spin-chain interactions and pronounced quantum fluctuations, can exhibit physical behaviors rarely observed in conventional high-dimensional magnets, such as Luttinger liquid states, charge density waves, exotic polaron resonances, and distinctive spin transport phenomena [27–30]. Q-1D materials have attracted considerable attention due to their structurally simpler frameworks, which offer an ideal platform for exploring strongly correlated electron phenomena. The two-leg ladder BaFe₂S₃ is a Mott insulator, exhibits stripe-type AFM order below 250 K, and undergoes a Mott transition followed by superconductivity under high pressure [31]. In contrast, the two-leg ladder BaFe₂Se₃ exhibits a robust block-type AFM order [32]. Notably, BaFe₂Se₃ distinguishes itself by its capability to host a rare type of orbital-selective Mott phase (OSMP), a characteristic absent in its isostructural counterpart BaFe₂S₃ [13,33–35]. Similarly, BaFe₂Se₃ can also be induced into a superconducting phase under high pressure [32]. Strictly speaking, the crystal structure of these two-leg ladder materials lies between 1D and 2D, which increases the structural complexity between interchain and intrachain. More recently, a canted AFM structure has been reported in Q-1D BaFe₂Se₄, which reduced the structural complexity of the two-leg ladder in BaFe₂Se₃ to a real single iron-chain configuration [36]. This edge-sharing single chain structure shows the evolution from the block-type AFM state in BaFe₂Se₃ to a canted AFM structure with a net moment along the *b* axis, driven by enhanced electronic correlations and reduced dimensionality. In

*These authors contributed equally to this work.

†Contact author: blv@utdallas.edu

addition to BaFe_2Se_3 , it has been reported that Q-1D edge-shared single chain $\text{K}_3\text{Fe}_2\text{Se}_4$ exhibits a block-type AFM structure [37]. All of the above materials, including the ladder phase and the single chain phase, contain edge-shared FeSe_4 chains. However, due to the geometric connectivity of the edge-shared FeSe_4 tetrahedra, there is still significant orbital overlap along the chain direction. In this context, a Q-1D material with a corner-shared FeSe_4 single chain structure would serve as a more suitable model system for elucidating the evolution of magnetism in iron chalcogenides, owing to its reduced orbital overlap and enhanced 1D character.

In this work, we extend the family of Q-1D iron chalcogenides by investigating the magnetic structure and physical properties of the corner-shared FeSe_4 linear single chain Ba_2FeSe_3 . We demonstrate the narrow gap semiconductor Ba_2FeSe_3 orders AFM below $T_N \sim 60$ K and have a canted AFM structure with a commensurate propagation vector of $\mathbf{k} = (0, \frac{1}{2}, 0)$. The Fe ion spins are arranged antiparallel along the Q-1D iron chain direction of the b axis, forming a robust up-down-up-down ($\uparrow - \downarrow - \uparrow - \downarrow$) AFM structure, in good agreement with density functional theory (DFT) calculations.

II. EXPERIMENTAL DETAILS

A. Sample synthesis, crystal structure, and physical property characterization

Ba_2FeSe_3 was prepared via the solid-state reaction method under ambient pressure. The high-quality polycrystalline powder sample of Ba_2FeSe_3 was synthesized using FeSe_3 precursor and Ba pieces (99.9%, Alfa Aesar) in a stoichiometric ratio inside an argon glove box with a total moisture and oxygen level <0.1 ppm. The FeSe_3 precursor was synthesized first using Fe granules (99.98%, Alfa Aesar) and Se shot (99.999%, Alfa Aesar) in a 1:3.06 ratio which was mixed and flame-sealed under vacuum. The 2% extra Se was to make sure no trace of elemental Fe remains unreacted. The ampoule was then heated to 800 °C for 1 d in a box furnace. The FeSe_3 precursor was then mixed with Ba pieces in a stoichiometric ratio, and the mixtures were transferred into a graphite crucible, followed by a vacuum seal inside a quartz tube. To slow down the exothermic reaction between Ba and residual Se, the ampoule was held at 200 and 500 °C for 5 h, respectively, and then reacted at 900 °C for 72 h. This black powder was reground and annealed at 750 °C for 1 wk and two times, to ensure the homogeneity of the sample. No Fe-based binary phases were presented in the sample, while a trace of highly stable phase BaSe existed, which is nonmagnetic and does not interfere with the magnetic structure determination. The polycrystalline powder sample was characterized by room-temperature x-ray diffraction (XRD) using a Rigaku Smartlab diffractometer of Cu K radiation. The crystal structural Rietveld refinements were carried out using GSAS-II packages [38]. Note that Ba_2FeSe_3 is air sensitive, so some nonreactive grease was used to protect the sample during the XRD measurement, and the peaks from the grease have been removed from the raw data before the refinements. VESTA software was used to plot crystal and magnetic structures. The DC magnetic susceptibility $\chi(T)$ and magnetization $M(B)$

were measured using a Quantum Design Magnetic Property Measurement System (MPMS) with the temperature down to 2 K and the magnetic field up to 5 T. The electrical resistivity $\rho(T)$ was measured with Quantum Design Physical Property Measurement System (PPMS) using the standard four-wire method on an annealed pellet made from the powder of Ba_2FeSe_3 .

B. Neutron powder diffraction

The temperature-dependent neutron powder diffraction (NPD) data were collected on 2 g fine powder using HB-2A with Ge (113) monochromator reflection, giving a wavelength of 2.41 Å at the High Flux Isotope Reactor (HFIR), Oak Ridge National Laboratory (ORNL) [39]. Magnetic structure determination was performed by Rietveld refinement of the NPD data by using FullProf Suite software, combined with representational analysis as implemented in the SARAH code [40] and the Bilbao Crystallographic Server.

C. DFT calculation

The first-principles DFT calculations were using the projector augmented-wave method, as implemented in VASP[41–43]. The generalized gradient approximation with the Perdew-Burke-Ernzerhof functional [44] was used to treat electronic exchange and correlation. To incorporate on-site Coulomb interactions in the Fe 3d orbitals, we employed the LSDA+U method in the Dudarev formalism [45]. The plane-wave energy cutoff was set to 500 eV, and the smallest allowed spacing between k points in the Brillouin zone sampling was set to 0.2 \AA^{-1} . All calculations were performed on the experimentally determined crystal structure from neutron diffraction measurements.

III. RESULTS AND DISCUSSION

A. Crystal structure, resistivity, and magnetic properties

Ba_2FeSe_3 crystallizes in the centrosymmetric $Pnma$ (No. 62) orthorhombic structure [46,47], as shown in Fig. 1(a). The XRD pattern for K_2CuCl_3 -type Ba_2FeSe_3 powder measured at room temperature and the corresponding structural refinement results are shown in Fig. 1(b) and Table S1 in the Supplemental Material [46]. Incorporating the minor impurity phase of BaSe in Rietveld refinement gives the errors of the profile factor $R_p = 2.60\%$, the errors of the weighted profile factor $R_{wp} = 2.30\%$, and the reduced $\chi^2 = 3.43$ with all the peaks indexed accurately. The Rietveld refinement result suggests orthorhombic structure with $a = 12.525(2)$ Å, $b = 4.407(8)$ Å, and $c = 12.869(6)$ Å. As shown in Fig. S1 in the Supplemental Material [46], contrary to the edge-shared FeSe_4 single chain BaFe_2Se_4 and two-leg ladder BaFe_2Se_3 , Ba_2FeSe_3 has a linear 1D single chain of corner-shared FeSe_4 distorted tetrahedra along the b axis separated by Ba atoms. The corner-shared chain configuration results in longer Fe–Fe bonds, which in 1D systems reduces electrical conductivity and tends to induce structural distortions, thereby giving rise to unusual magnetic behavior. The inter-chain distance between neighboring Fe–Fe atoms is 6.831(2) Å along the c direction and 6.325(3) Å along the a direction,

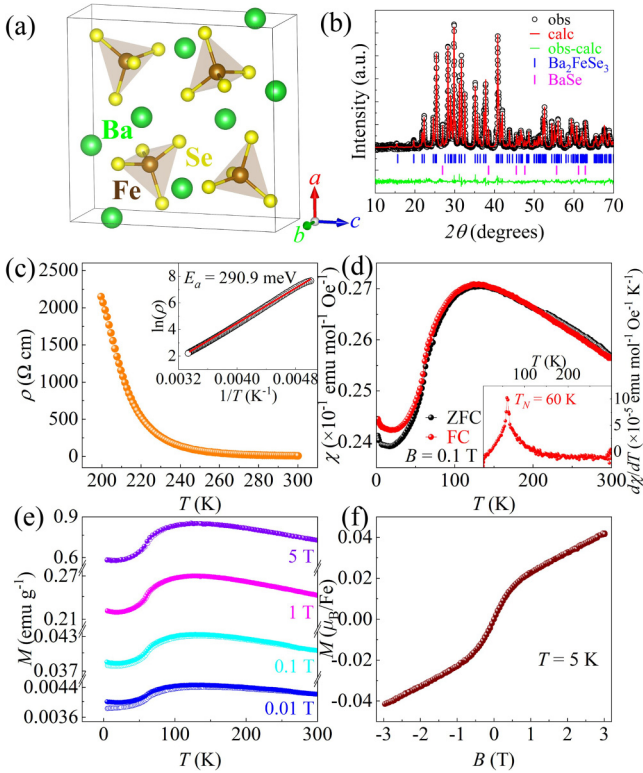


FIG. 1. (a) Schematic crystal structure of the Ba₂FeSe₃ conventional unit cell, where green atom represents Ba, brown atom represents Fe, and yellow atom represents Se, respectively. (b) The powder XRD pattern of Ba₂FeSe₃ measured at room temperature and the Rietveld refinement results. (c) Temperature-dependent electrical resistivity of Ba₂FeSe₃ and the inset showing linear fitting of $\ln(\rho)$ vs $1/T$. (d) Temperature-dependent magnetic susceptibility $\chi(T)$ of Ba₂FeSe₃ measured with ZFC and FC modes. Inset shows the first derivative of the FC mode temperature-dependent $\chi(T)$ curve, indicating the AFM transition temperature of 60 K. (e) Magnetization as a function of temperature in the FC (closed) and ZFC (open) mode at various applied fields. (f) Magnetic hysteresis loop at 5 K.

significantly longer than other single chain phases BaFe₂Se₄ [36] and K₃Fe₂Se₄ [37]. However, the intrachain distance between Fe–Fe atoms is 4.439(2) Å and constant along the *b*-axis chain direction. This structure indicates that the intrachain interaction is dominant, while the interchain interaction has a weak influence. The tetrahedral unit is also not symmetric concerning the Fe–Se distance. The two Fe–Se bonds along the chain direction are 2.563(9) Å, while the remaining two are 2.381(8) and 2.435(1) Å. The intrachain Fe–Fe bond distances are around 50% larger than those of edge-shared single chain BaFe₂Se₄ or two-leg ladder BaFe₂Se₃ [32–34,36], indicating lesser overlap of tetrahedral units consistent with the corner-sharing model.

The temperature-dependent electrical resistivity of polycrystalline Ba₂FeSe₃ is shown in Fig. 1(c). The electrical resistivity shows semiconducting behavior approaching the upper limit of the measurement range in our PPMS instrument around 200 K. The inset of Fig. 1(c) shows the results of linear fitting of $\ln(\rho)$ vs $1/T$, which is consistent with the standard activation model $\rho = \rho_0 \exp(E_a/k_B T)$ [36,48]. The activation energy E_a estimated from the fitting is $E_a = 290.9$ meV, which

is higher than the reported gap value of Q-1D linear iron chain BaFe₂Se₄ (~ 142.5 meV) and Q-1D two-leg ladder BaFe₂Se₃ (~ 180 meV). The room temperature electrical resistivity is ~ 9.1 Ω cm of Ba₂FeSe₃, which is much higher than Q-1D two-leg ladder BaFe₂Se₃ ~ 0.35 Ω cm [13] but lower than Q-1D two-leg ladder BaFe₂Se₃ ~ 17 Ω cm and Q-1D edge-shared linear iron chain BaFe₂Se₄ ~ 35.5 Ω cm [36,48,49]. Note that this is the polycrystalline powder electrical resistivity, and a large anisotropy in direction-dependent resistivity of a single crystal is expected due to its Q-1D structure.

The temperature dependence of magnetic susceptibility $\chi(T)$ from 2 to 350 K under zero-field-cooled (ZFC) and field-cooled (FC) procedures is shown in Figs. 1(d) and 1(e). We observe that $\chi(T)$ at low applied fields is similar to that at applied fields up to 5 T. In the higher-temperature region, $\chi(T)$ gradually increases as the temperature decreases and does not conform to the Curie-Weiss law. The broad hump observed around ~ 125 K is reminiscent of similar behavior observed in Ba₂CoS₃, Ba₂MnS₃, and Ba₂FeS₃ [50–53], which is typical of Q-1D AFMs with short-range interactions. This may indicate intrachain short-range AFM interactions preceding the long-range magnetic order, and the detailed origin of this hump is discussed later in the neutron diffraction analysis. In the lower-temperature region, $\chi(T)$ gradually increases but does not show any sharp abnormality. The derivative of the magnetic susceptibility vs temperature curve shows that Ba₂FeSe₃ undergoes a paramagnetic (PM)-to-AFM transition at 60 K, as shown in the inset of Fig. 1(d). When the applied field increases, the broad hump still exists but moves toward higher temperature, as shown in Fig. 1(e). As shown in Fig. 1(f), we do not observe any hysteresis in the magnetization as a function of field $M(B)$ curve. However, it is important to note that magnetization values in the $M(B)$ curve follow a nonlinear trend consistent with the $\chi(T)$ curve. The magnetization value is approximately 0.042 μ_B/Fe at 3 T, which is much smaller than the theoretical saturation value of the Fe ion, indicating the magnetic moments still maintain AFM alignment.

B. NPD and magnetic structure

To further investigate the magnetic properties, we have performed NPD measurements at several temperatures between 200 and 2 K to determine the magnetic structure of Ba₂FeSe₃. Figure 2(a) and Fig. S2(b) in the Supplemental Material [46] illustrate the diffraction pattern of HB-2A measured with a wavelength of 2.41 Å at 200 and 100 K, respectively. It corresponds well to the nuclear crystal structure, indicating that no structural transition occurs. Figures 2(b) and 2(c) represent the diffraction pattern measured at 40 and 2 K, in which the additional Bragg peaks unindexed by the nuclear unit cell indicate long-range magnetic order with a nonzero *k* vector. The position of magnetic peaks at 40 and 2 K is consistent, and the position of magnetic peaks can be clearly seen in the partially enlarged diffraction pattern in Fig. 2(d). Figure 2(e) shows the intensity of the new low *Q* magnetic peak as a function of temperature, showing that the peak intensity arises below 60 K, consistent with the AFM transition feature observed in the magnetization measurements. SARAH and the Bilbao Crystallographic Server were employed to determine

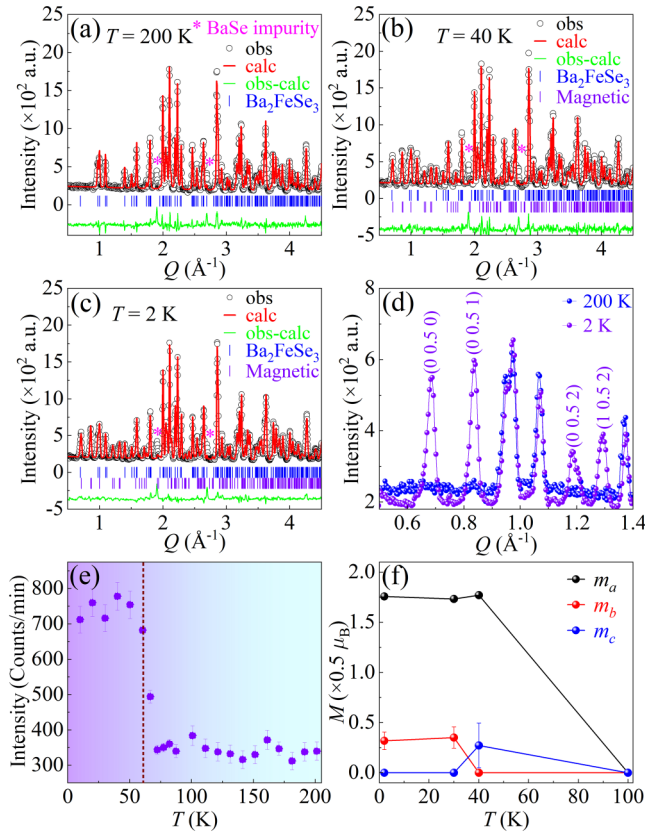


FIG. 2. NPD pattern and Rietveld refinement results of Ba_2FeSe_3 at (a) $T = 200$ K, (b) $T = 40$ K, and (c) $T = 2$ K. (d) Magnetic peaks evolved at $T = 2$ K as compared with no magnetic peaks at $T = 200$ K. (e) The intensity of first magnetic peak (0 0.5 0) as a function of temperature. The brown dotted line represents the AFM transition temperature of 60 K. (f) The components of the Fe magnetic moments along the a , b , and c axes as a function of temperature obtained from NPD data.

the magnetic structure of Ba_2FeSe_3 [40]. Considering the nuclear unit cell, the magnetic peaks are all indexable by a doubling of the b lattice parameter, indicating a commensurate ordering wave vector $\mathbf{k} = (0, \frac{1}{2}, 0)$. We performed a full representational analysis for NPD data at 2 K to determine possible irreducible representations (irreps) and basis vectors (BVs) that describe the magnetic structure using the SARAH code. For $\mathbf{k} = (0, \frac{1}{2}, 0)$ in the $Pnma$ space group with the magnetic Fe ion on the $4c$ Wyckoff position case, there are two possible irreps, each having six BVs, where Fe1, Fe2, Fe3, and Fe4 are the four symmetry-related Fe sites in the nuclear unit cell; the detailed irreps and BVs are categorized in Table S2 in the Supplemental Material [46]. For each irrep Γ , linear combinations of the BVs were used to correlate the irreps with maximal symmetry magnetic space groups. This produced four possible magnetic structures with three BVs per structure. For the magnetic space groups $Pamn21$ (BNS No. 26.71) and $Pamc21$ (BNS No. 31.128) cases, the symmetry constrained two of the Fe positions to have moments only along the b axis and the other two positions to have moments in the ac plane. The remaining two structures were both of magnetic space group $Pa21/c$ (BNS No. 14.80) and allowed

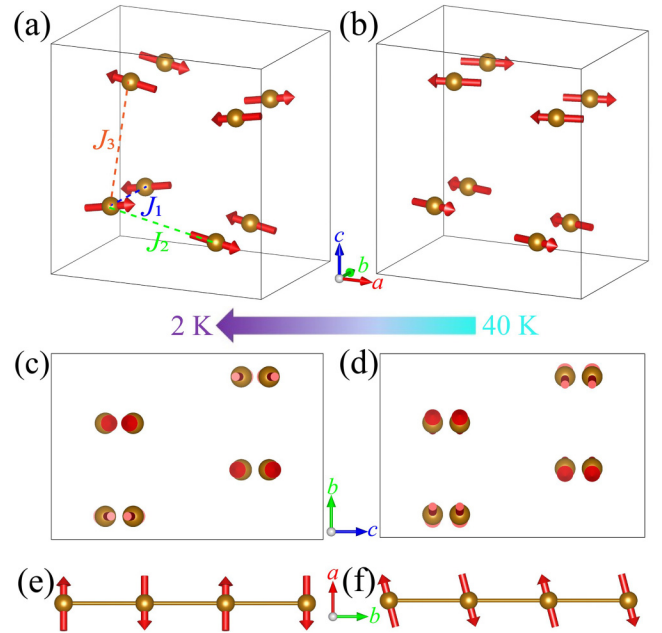


FIG. 3. Schematic magnetic structure of Ba_2FeSe_3 . Canted AFM structure at (a) and (c) $T = 2$ K and (b) and (d) $T = 40$ K. The $\uparrow - \downarrow - \uparrow - \downarrow$ -type spin alignment along the 1D iron chain direction of the b axis at (e) $T = 2$ K and (f) $T = 40$ K. Black lines represent the magnetic unit cell, which is twice as large as the crystal unit cell.

all the Fe positions to have moment components in both a and c directions. Of these, only the latter adequately modeled the observed intensities with the best fitting structure belonging to Γ_2 with $Pa21/c$, and the obtained magnetic structure at 2 K is shown in Figs. 3(a) and 3(c). The refined magnetic moment at 2 K estimated from NPD data is $3.57 \mu_B/\text{Fe}$, and the magnetic mode of Ba_2FeSe_3 at 2 K is shown in Table S4 in the Supplemental Material [46]. The total magnetic moment value lies between the high-spin Fe^{3+} state and the low-spin Fe^{2+} state according to crystal field theory, which suggests a mixing of states in Ba_2FeSe_3 , as observed in BaFe_2Se_3 and BaFe_2Se_4 [36,54,55]. In the ac plane, the tilting angle between adjacent Fe ion moments is 20° , and each spin deviates from the a axis by 10° . As shown in Fig. 3(a), the Γ_2 fitting suggests the intrachain nearest-neighboring (NN) AFM interaction (J_1) along the b axis and the interchain FM interaction (J_2) along the a axis, which indicates Ba_2FeSe_3 has canted AFM with AFM and FM spin alignment along a perpendicular direction. Each Fe ion spin is coupled with AFM along the chain direction of the b axis and canted AFM alignment along the c axis but canted FM alignment along the a axis, showing a $\uparrow - \downarrow - \uparrow - \downarrow$ -type canted AFM structure with zero net magnetization. These kinds of FM and AFM interactions emphasize the dominance of short-range interactions of the NN and next-NNs (NNNs) [35]. These short-range interchain and intrachain exchange interactions exist before the onset of long-range AFM orders in 3D, corresponding to the broad hump that occurs in the high-temperature region of the $\chi(T)$ curve. Even though our system is an isolated chain of FeSe_4 tetrahedra, the magnetic interactions due to the NNNs cause deviation from the Curie-Weiss behavior above $T_N \sim 60$ K, similar to the Heisenberg AFM system Ba_2CoS_3 [56].

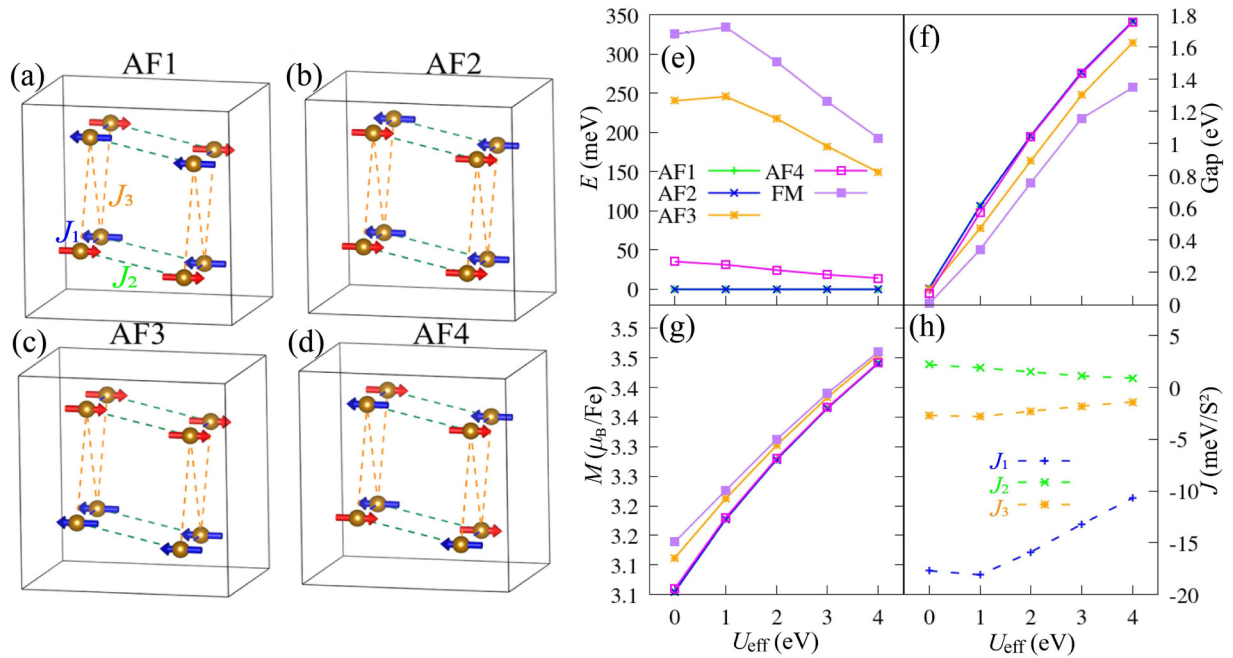


FIG. 4. Sketches of some magnetic configurations studied in DFT calculations. (a) AF1 state with $J_1 < 0$, $J_2 > 0$, and $J_3 < 0$. (b) AF2 state with $J_1 < 0$, $J_2 > 0$, and $J_3 > 0$. (c) AF3 state with $J_1 > 0$, $J_2 > 0$, and $J_3 < 0$. (d) AF4 state with $J_1 < 0$, $J_2 < 0$, and $J_3 < 0$. DFT results for Ba_2FeSe_3 as a function of the Hubbard U_{eff} coupling. (e) Energies of various magnetic orders. The AF1 configuration is taken as the reference. (f) Band gaps for the many magnetic states analyzed. (g) Local magnetic moments of Fe, integrated within the default Wigner-Seitz sphere as defined by VASP. (h) Magnetic exchange couplings as a function of the Hubbard U_{eff} coupling.

Note that, in the order parameter scan, we do not see clear evidence of a change in intensity below T_N shown in Fig. 2(e), which corresponds to the $\chi(T)$ curve not showing significant change in intensity at the transition temperature, as shown in Fig. 1(d).

Interestingly, although no anomalies were observed in the $M(T)$ curve, we do see evidence of spin-reorientation in our Rietveld modeling of the full neutron diffraction patterns, i.e., nonmonotonic behavior of spin orientation below 40 K. First, we observe this behavior in raw intensities of the temperature-dependent magnetic peaks, specifically the second peak, as seen in Fig. S3 in the Supplemental Material [46]; the intensity of 30 K is less than that of both 40 and 2 K. Furthermore, an interchange between m_a and m_b is observed with decreasing temperature, signifying a nonmonotonic behavior where the canted spins reorient from the c axis to the b axis on further cooling [see Figs. 2(f) and 3(a)–3(d)]. However, the spin arrangement at 30 and 2 K is basically the same, as shown in Fig. 3 and Table S4 in the Supplemental Material [46]. The $\uparrow - \downarrow - \uparrow - \downarrow$ -type canted AFM structure in Ba_2FeSe_3 is different than the typical block- or stripe-type AFM structure observed in two-leg ladder Q-1D BaFe_2Se_3 and BaFe_2S_3 [32,34,57]. In addition to the two-leg spin-ladder material, for comparison, the Q-1D edge-shared iron chain magnet BaFe_2Se_4 has a canted AFM state at 2 K with the magnetic moment AFM alignment along the b axis, while the tilting angle is 18.7° from the a axis [36]. The Q-1D edge-shared iron chain $\text{K}_3\text{Fe}_2\text{Se}_4$ exhibits a block-type canted AFM structure below 110 K [37]. When the perspective shifts to the corner-shared chain magnet with enhanced 1D features, compared with Q-1D corner-shared Co chain Ba_2CoS_3 , it has a collinear AFM structure with commensurate propagation

vector $\mathbf{k} = (0, 0, \frac{1}{2})$, where the spins lie in the ac plane and the neighboring spins in each Co chain of the c axis couple AFM [56]. Q-1D corner-shared Mn chain magnet Ba_2MnS_3 has a commensurate AFM structure with propagation vector $\mathbf{k} = (0, \frac{1}{2}, 0)$; the nearest spin chains are FM coupling, while the next nearest spin chains are AFM coupling [58]. The spin-reorientation phenomenon in Ba_2FeSe_3 is different than other corner- and edge-shared chain materials; it is closely related to the corner-shared configuration and reflects the strong 1D characteristics in Ba_2FeSe_3 . Further studies such as inelastic neutron scattering experiments are required to unveil the exchange interactions for a deep understanding of the canted AFM structure and spin reorientation in Q-1D single chain Ba_2FeSe_3 .

C. DFT calculation and magnetic ground state

To better understand the magnetic ground state, both FM and several AFM configurations were considered using a $1 \times 2 \times 1$ supercell, as illustrated in Figs. 4(a)–4(d). For simplicity, only the collinear patterns are considered. The AF1 state, staggered $\uparrow - \downarrow - \uparrow - \downarrow$ AFM state along chain direction, is consistent with our NPD experiment. As shown in Fig. 4(e), the AF1 and AF2 magnetic configurations are nearly degenerate and consistently have the lowest energy among all tested states, regardless of the value of U_{eff} . As illustrated in Fig. 4(f), all AFM orders are insulators, and the band gap increases with U_{eff} , with the experimental gap of 290.9 meV falling between the values $U_{\text{eff}} = 0$ and 1 eV. As shown in Fig. 4(g), the Fe magnetic moment in the AF1/AF2 states increases from 3.105 to 3.491 μ_B/Fe as U_{eff} increases, in good agreement with the

experimental value of $3.57 \mu_B/\text{Fe}$ at 2 K obtained from NPD data.

To extract magnetic exchange parameters, we mapped the DFT energies of various magnetic configurations into a classical Heisenberg model

$$H = -J_1 \sum_{\langle i,j \rangle} \mathbf{S}_i \cdot \mathbf{S}_j - J_2 \sum_{[k,l]} \mathbf{S}_k \cdot \mathbf{S}_l - J_3 \sum_{\{m,n\}} \mathbf{S}_m \cdot \mathbf{S}_n. \quad (1)$$

Here, J_1 denotes the intrachain exchange interaction between NN Fe–Fe spin pairs, while J_2 and J_3 correspond to two types of interchain NN interactions, as illustrated in Figs. 3(a) and 4(a). The extracted values of J_1 , J_2 , and J_3 as a function of U_{eff} are shown in Fig. 4(h). As expected, J_1 is dominant, confirming that Ba_2FeSe_3 favors the AFM pattern along the chain direction, while interchain couplings J_2 and J_3 are significantly weaker. For example, at $U_{\text{eff}} = 1 \text{ eV}$, $J_1 = -18.1$, $J_2 = 1.9$, and $J_3 = -2.8$ in units of meV/S^2 , implying weakly competing FM and AFM interactions between and within iron chains. Our DFT results suggest the dominant staggered $\uparrow - \downarrow - \uparrow - \downarrow$ AFM state along the chain direction is stable at many values of U_{eff} , and this situation is similar to the previous studies on the high-pressure phase of Ba_2FeS_3 [59].

IV. CONCLUSIONS

In summary of our experimental and theoretical calculation results, we found the canted AFM state together with spin reorientation in Q-1D iron chalcogenide with corner-shared FeSe_4 single chain of Ba_2FeSe_3 . The narrow-gap semiconductor Ba_2FeSe_3 exhibits weak short-range magnetic coupling in the PM region and orders AFM below 60 K. Neutron diffraction results reveal that Ba_2FeSe_3 has a canted AFM structure of space group $Pa21/c$ (BNS No. 14.80) with the commensurate propagation vector $\mathbf{k} = (0, \frac{1}{2}, 0)$, forming a dominant staggered $\uparrow - \downarrow - \uparrow - \downarrow$ spin alignment along the b axis. The spin structure exhibits a slight spin reorientation upon cooling in the magnetically ordered state, with the spins reoriented from the ab plane to the ac plane upon cooling. The DFT calculation results suggest the dominant $\uparrow - \downarrow - \uparrow - \downarrow$ AFM state is stable at many values of U_{eff} . The corner-shared

FeSe_4 tetrahedra and linear single iron chain Q-1D structure with very little orbital overlap in this compound provides an ideal platform to explore the interplay between magnetism, electrical transport, Fe-valency, and exotic physical behavior under high pressures.

ACKNOWLEDGMENTS

This work at the University of Texas at Dallas was supported by the U.S. Air Force Office of Scientific Research (Grant No. FA9550-19-1-0037), National Science Foundation (Grants No. DMR-DMREF-2324033 and No. ECCS-2516364), and Office of Naval Research (Grant No. N00014-23-1-2020). The work of L.L., Y.Z. and E.D. was supported by the U.S. Department of Energy (DOE), Office of Science, Basic Energy Sciences, Materials Sciences and Engineering Division. This research used resources at the High Flux Isotope Reactor, a DOE Office of Science User Facility operated by the Oak Ridge National Laboratory. The neutron diffraction experiments were conducted on the HB-2A powder diffractometer (Proposal No. IPTS-26330). This research used resources of the Advanced Photon Source, a DOE Office of Science User Facility operated for the DOE Office of Science by Argonne National Laboratory under Contract No. DE-AC02-06CH11357. The submitted manuscript has been created by UChicago Argonne, LLC, Operator of Argonne National Laboratory (“Argonne”). Argonne, a U.S. Department of Energy Office of Science laboratory, is operated under Contract No. DE-AC02-06CH11357. The U.S. Government retains for itself, and others acting on its behalf, a paid-up nonexclusive, irrevocable worldwide license in said article to reproduce, prepare derivative works, distribute copies to the public, and perform publicly and display publicly, by or on behalf of the Government. The Department of Energy will provide public access to these results of federally sponsored research in accordance with the DOE Public Access Plan [61].

DATA AVAILABILITY

The data that support the findings of this article are openly available [62].

-
- [1] Y. Kamihara, T. Watanabe, M. Hirano, and H. Hosono, Iron-based layered superconductor $\text{La}[\text{O}_{1-x}\text{F}_x]\text{FeAs}$ ($x = 0.05\text{--}0.12$) with $T_c = 26 \text{ K}$, *J. Am. Chem. Soc.* **130**, 3296 (2008).
- [2] K. Sasmal, B. Lv, B. Lorenz, A. M. Guloy, F. Chen, Y.-Y. Xue, and C.-W. Chu, Superconducting Fe-based compounds $(\text{A}_{1-x}\text{Sr}_x)\text{Fe}_2\text{As}_2$ with $A = \text{K}$ and Cs with transition temperatures up to 37 K, *Phys. Rev. Lett.* **101**, 107007 (2008).
- [3] J. H. Tapp, Z. Tang, B. Lv, K. Sasmal, B. Lorenz, P. C. W. Chu, and A. M. Guloy, LiFeAs : An intrinsic FeAs-based superconductor with $T_c = 18 \text{ K}$, *Phys. Rev. B* **78**, 060505(R) (2008).
- [4] K. Sasmal, B. Lv, Z. J. Tang, F. Chen, Y. Y. Xue, B. Lorenz, A. M. Guloy, and C. W. Chu, Unusual doping dependence of superconductivity in Na_xFeAs , *Phys. Rev. B* **79**, 184516 (2009).
- [5] M. D. Lumsden and A. D. Christianson, Magnetism in Fe-based superconductors, *J. Phys.: Condens. Matter* **22**, 203203 (2010).
- [6] F.-C. Hsu, J.-Y. Luo, K.-W. Yeh, T.-K. Chen, T.-W. Huang, P. M. Wu, Y.-C. Lee, Y.-L. Huang, Y.-Y. Chu, D.-C. Yan, *et al.*, Superconductivity in the PbO-type structure $\alpha\text{-FeSe}$, *Proc. Natl. Acad. Sci. USA* **105**, 14262 (2008).
- [7] G. R. Stewart, Superconductivity in iron compounds, *Rev. Mod. Phys.* **83**, 1589 (2011).
- [8] P. C. Dai, J. P. Hu, and E. Dagotto, Magnetism and its microscopic origin in iron-based high-temperature superconductors, *Nat. Phys.* **8**, 709 (2012).
- [9] E. Dagotto, The unexpected properties of alkali metal iron selenide superconductors, *Rev. Mod. Phys.* **85**, 849 (2013).
- [10] I. I. Mazin, D. J. Singh, M. D. Johannes, and M. H. Du, Unconventional superconductivity with a sign reversal in the or-

- der parameter of $\text{LaFeAsO}_{1-x}\text{F}_x$, *Phys. Rev. Lett.* **101**, 057003 (2008).
- [11] K. Kuroki, S. Onari, R. Arita, H. Usui, Y. Tanaka, H. Kontani, and H. Aoki, Unconventional pairing originating from the disconnected Fermi surfaces of superconducting $\text{LaFeAsO}_{1-x}\text{F}_x$, *Phys. Rev. Lett.* **101**, 087004 (2008).
- [12] S. X. Chi, Y. Uwatoko, H. B. Cao, Y. Hirata, K. Hashizume, T. Aoyama, and K. Ohgushi, Magnetic precursor of the pressure-induced superconductivity in Fe-ladder compounds, *Phys. Rev. Lett.* **117**, 047003 (2016).
- [13] P. C. Dai, Antiferromagnetic order and spin dynamics in iron-based superconductors, *Rev. Mod. Phys.* **87**, 855 (2015).
- [14] M. H. Christensen, B. M. Andersen, and P. Kotetes, Unravelling incommensurate magnetism and its emergence in iron-based superconductors, *Phys. Rev. X* **8**, 041022 (2018).
- [15] E. Dagotto, Experiments on ladders reveal a complex interplay between a spin-gapped normal state and superconductivity, *Rep. Prog. Phys.* **62**, 1525 (1999).
- [16] V. J. Emery, S. A. Kivelson, and J. M. Tranquada, Stripe phases in high-temperature superconductors, *Proc. Natl. Acad. Sci. USA* **96**, 8814 (1999).
- [17] P. A. Lee, N. Nagaosa, and X.-G. Wen, Doping a Mott insulator: Physics of high-temperature superconductivity, *Rev. Mod. Phys.* **78**, 17 (2006).
- [18] H. Ryu, H. C. Lei, A. I. Frenkel, and C. Petrovic, Local structural disorder and superconductivity in $\text{K}_x\text{Fe}_{2-y}\text{Se}_2$, *Phys. Rev. B* **85**, 224515 (2012).
- [19] L. S. Li, L. L. Zheng, B. A. Frandsen, A. D. Christianson, D.-X. Yao, M. Wang, and R. J. Birgeneau, Spin dynamics of the spin-chain antiferromagnet RbFeS_2 , *Phys. Rev. B* **104**, 224419 (2021).
- [20] J. Ying, H. C. Lei, C. Petrovic, Y. Xiao, and V. V. Struzhkin, The interplay of magnetism and superconductivity in compressed Fe-ladder compound BaFe_2Se_3 , *Phys. Rev. B* **95**, 241109(R) (2017).
- [21] S. A. J. Kimber, A. Kreyssig, Y.-Z. Zhang, H. O. Jeschke, R. Valentí, F. Yokaichiya, E. Colombier, J. Q. Yan, T. C. Hansen, T. Chatterji, *et al.*, Similarities between structural distortions under pressure and chemical doping in superconducting BaFe_2As_2 , *Nat. Mater.* **8**, 471 (2009).
- [22] M. Gooch, B. Lv, L. Z. Deng, T. Muramatsu, J. Meen, Y. Y. Xue, B. Lorenz, and C. W. Chu, High-pressure study of superconducting and nonsuperconducting single crystals of the same nominal composition $\text{Rb}_{0.8}\text{Fe}_2\text{Se}_2$, *Phys. Rev. B* **84**, 184517 (2011).
- [23] M. Yi, D. H. Lu, R. Yu, S. C. Riggs, J.-H. Chu, B. Lv, Z. K. Liu, M. Lu, Y.-T. Cui, M. Hashimoto, *et al.*, Observation of temperature-induced crossover to an orbital-selective Mott phase in $\text{A}_x\text{Fe}_{2-y}\text{Se}_2$ ($A = \text{K}, \text{Rb}$) superconductors, *Phys. Rev. Lett.* **110**, 067003 (2013).
- [24] S. Okamoto and A. J. Millis, Theory of Mott insulator-band insulator heterostructures, *Phys. Rev. B* **70**, 075101 (2004).
- [25] M. Tsuchiizu, Y. Fuseya, Y. Suzumura, and C. Bourbonnais, Dimensionality effect in quasi-one-dimensional Mott insulators, *J. Low Temp. Phys.* **142**, 651 (2006).
- [26] J.-K. Bao, J.-Y. Liu, C.-W. Ma, Z.-H. Meng, Z.-T. Tang, Y.-L. Sun, H.-F. Zhai, H. Jiang, H. Bai, C.-M. Feng, *et al.*, Superconductivity in quasi-one-dimensional $\text{K}_2\text{Cr}_3\text{As}_3$ with significant electron correlations, *Phys. Rev. X* **5**, 011013 (2015).
- [27] N. Wakeham, A. F. Bangura, X. F. Xu, J.-F. Mercure, M. Greenblatt, and N. E. Hussey, Gross violation of the Wiedemann-Franz law in a quasi-one-dimensional conductor, *Nat. Commun.* **2**, 396 (2011).
- [28] Y. Zhang, R. Zhou, H. Wu, J. S. Oh, S. Li, J. Huang, J. D. Denlinger, M. Hashimoto, D. Liu, S.-K. Mo, *et al.*, Charge order induced Dirac pockets in the nonsymmorphic crystal TaTe_4 , *Phys. Rev. B* **108**, 155121 (2023).
- [29] T. Uto, B. Evrard, K. Watanabe, T. Taniguchi, M. Kroner, and A. İmamoğlu, Interaction-induced ac Stark shift of exciton-polaron resonances, *Phys. Rev. Lett.* **132**, 056901 (2024).
- [30] G. S. Murugan, S. Lee, C. Wang, H. Luetkens, K.-Y. Choi, and R. Sankar, Spin dynamics of the one-dimensional double chain spin- $\frac{1}{2}$ antiferromagnet $\text{KNaCuP}_2\text{O}_7$, *Phys. Rev. B* **105**, 174442 (2022).
- [31] T. Yamauchi, Y. Hirata, Y. Ueda, and K. Ohgushi, Pressure-induced Mott transition followed by a 24-K superconducting phase in BaFe_2S_3 , *Phys. Rev. Lett.* **115**, 246402 (2015).
- [32] S. Wu, J. J. Yin, T. Smart, A. Acharya, C. L. Bull, N. P. Funnell, T. R. Forrest, G. Simutis, R. Khasanov, S. K. Lewin, *et al.*, Robust block magnetism in the spin ladder compound BaFe_2Se_3 under hydrostatic pressure, *Phys. Rev. B* **100**, 214511 (2019).
- [33] L. Craco and S. Leoni, Pressure-induced orbital-selective metal from the Mott insulator BaFe_2Se_3 , *Phys. Rev. B* **101**, 245133 (2020).
- [34] M. Mourigal, S. Wu, M. B. Stone, J. R. Neilson, J. M. Caron, T. M. McQueen, and C. L. Broholm, Block magnetic excitations in the orbitally selective Mott insulator BaFe_2Se_3 , *Phys. Rev. Lett.* **115**, 047401 (2015).
- [35] J. Herbrych, N. Kaushal, A. Nocera, G. Alvarez, A. Moreo, and E. Dagotto, Spin dynamics of the block orbital-selective Mott phase, *Nat. Commun.* **9**, 3736 (2018).
- [36] X. Y. Liu, K. M. Taddei, S. Li, W. H. Liu, N. Dhale, R. Kadado, D. Berman, C. D. Cruz, and B. Lv, Canted antiferromagnetism in the quasi-one-dimensional iron chalcogenide BaFe_2Se_4 , *Phys. Rev. B* **102**, 180403(R) (2020).
- [37] F. Gao, N. Dhale, L.-F. Lin, K. M. Taddei, Y. Zhang, C. D. Cruz, E. Dagotto, and B. Lv, Block-type antiferromagnetism in single chain quasi-one-dimensional $\text{K}_3\text{Fe}_2\text{Se}_4$ (unpublished).
- [38] B. H. Toby and R. B. Von Dreele, GSAS-II: The genesis of a modern open-source all purpose crystallography software package, *J. Appl. Crystallogr.* **46**, 544 (2013).
- [39] S. Calder, K. An, R. Boehler, C. R. Dela Cruz, M. D. Frontzek, M. Guthrie, B. Haberl, A. Huq, S. A. J. Kimber, J. Liu, *et al.*, A suite-level review of the neutron powder diffraction instruments at Oak Ridge National Laboratory, *Rev. Sci. Instrum.* **89**, 092701 (2018).
- [40] A. S. Wills, A new protocol for the determination of magnetic structures using simulated annealing and representational analysis (SARAH), *Phys. B* **276–278**, 680 (2000).
- [41] G. Kresse and J. Hafner, *Ab initio* molecular dynamics for liquid metals, *Phys. Rev. B* **47**, 558 (1993).
- [42] G. Kresse and J. Furthmüller, Efficient iterative schemes for *ab initio* total-energy calculations using a plane-wave basis set, *Phys. Rev. B* **54**, 11169 (1996).
- [43] P. E. Blöchl, Projector augmented-wave method, *Phys. Rev. B* **50**, 17953 (1994).
- [44] J. P. Perdew, K. Burke, and M. Ernzerhof, Generalized gradient approximation made simple, *Phys. Rev. Lett.* **77**, 3865 (1996).

- [45] S. L. Dudarev, G. A. Botton, S. Y. Savrasov, C. J. Humphreys, and A. P. Sutton, Electron-energy-loss spectra and the structural stability of nickel oxide: An LSDA+U study, *Phys. Rev. B* **57**, 1505 (1998).
- [46] See Supplemental Material at <http://link.aps.org/supplemental/10.1103/1b28-p1fr> for crystal structure, neutron diffraction experiments, and Rietveld refinement results details, which includes Ref. [60].
- [47] H. Y. Hong and H. Steinfink, The crystal chemistry of phases in the BaFeS and Se systems, *J. Solid State Chem.* **5**, 93 (1972).
- [48] H. C. Lei, H. Ryu, A. I. Frenkel, and C. Petrovic, Anisotropy in BaFe₂Se₃ single crystals with double chains of FeSe tetrahedra, *Phys. Rev. B* **84**, 214511 (2011).
- [49] B. Saparov, S. Calder, B. Sipos, H. B. Cao, S. X. Chi, D. J. Singh, A. D. Christianson, M. D. Lumsden, and A. S. Sefat, Spin glass and semiconducting behavior in one-dimensional BaFe_{2- δ} Se₃ ($\delta = 0.2$) crystals, *Phys. Rev. B* **84**, 245132 (2011).
- [50] N. Nakayama, K. Kosuge, and S. Kachi, Studies on the compounds in the Ba-Fe-S system. I. Linear chain antiferromagnetism of Ba₂FeS₃ and related compounds Ba₂CoS₃ and Ba₂MnS₃, *J. Solid State Chem.* **33**, 351 (1980).
- [51] T. Baikie, A. Maignan, and M. G. Francesconi, Linear antiferromagnetism in Ba₂CoS₃, *Chem. Commun.* **7**, 836 (2004).
- [52] A. D. J. Barnes, T. Baikie, V. Hardy, M.-B. Lepetit, A. Maignan, N. A. Young, and M. G. Francesconi, Magnetic coupling and long-range order in the spin-chain sulfide Ba₂CoS₃, *J. Mater. Chem.* **16**, 3489 (2006).
- [53] L. Duan, J. Zhang, X. C. Wang, Z. W. Zhao, C. J. Xiao, X. Li, Z. W. Hu, J. F. Zhao, W. M. Li, L. P. Cao, *et al.*, High pressure phase of Ba₂FeS₃: An antiferromagnet with one-dimensional spin chains, *J. Alloys Compd.* **859**, 157839 (2021).
- [54] Y. Nambu, K. Ohgushi, S. Suzuki, F. Du, M. Avdeev, Y. Uwatoko, K. Munakata, H. Fukazawa, S. X. Chi, Y. Ueda, *et al.*, Block magnetism coupled with local distortion in the iron-based spin-ladder compound BaFe₂Se₃, *Phys. Rev. B* **85**, 064413 (2012).
- [55] J. M. Caron, J. R. Neilson, D. C. Miller, K. Arpino, A. Llobet, and T. M. McQueen, Orbital-selective magnetism in the spin-ladder iron selenides Ba_{1-x}K_xFe₂Se₃, *Phys. Rev. B* **85**, 180405(R) (2012).
- [56] D. A. Headspith, P. D. Battle, and M. G. Francesconi, Long-range magnetic ordering in Ba₂CoS₃: A neutron diffraction study, *J. Solid State Chem.* **180**, 2859 (2007).
- [57] H. Takahashi, A. Sugimoto, Y. Nambu, T. Yamauchi, Y. Hirata, T. Kawakami, M. Avdeev, K. Matsubayashi, F. Du, C. Kawashima, *et al.*, Pressure-induced superconductivity in the iron-based ladder material BaFe₂S₃, *Nat. Mater.* **14**, 1008 (2015).
- [58] B. J. Moore, Z. X. Cui, Y. Liu, M. J. Gutmann, E. N. Teather, F. Orlandi, C. Balz, P. Manuel, and R. S. Perry, Crystal growth of ternary metal sulfides from an open melt: Ba₂MnS₃, *CrystEngComm* **26**, 1444 (2024).
- [59] Y. Zhang, L.-F. Lin, G. Alvarez, A. Moreo, and E. Dagotto, Magnetic states of the quasi-one-dimensional iron chalcogenide Ba₂FeS₃, *Phys. Rev. B* **104**, 125122 (2021).
- [60] M. R. Harrison and M. G. Francesconi, Mixed metal one-dimensional sulfides—A class of materials with differences and similarities to oxides, *Coordin. Chem. Rev.* **255**, 451 (2011).
- [61] <http://energy.gov/downloads/doe-public-access-plan>.
- [62] <https://doi.org/10.5281/zenodo.18445061>.